

A van der Waals antiferromagnetic topological insulator with weak interlayer magnetic coupling

Chaowei Hu¹, Xiaoqing Zhou², Pengfei Liu³, Jinyu Liu¹, Peipei Hao², Eve Emmanouilidou¹, Hongyi Sun³, Yuntian Liu³, Harlan Brawer¹, Arthur P. Ramirez⁴, Huibo Cao⁵, Qihang Liu^{3,6‡}, Dan Dessau^{2,7†}, and Ni Ni^{1*}

¹Department of Physics and Astronomy and California NanoSystems Institute, University of California, Los Angeles, CA 90095, USA

²Department of Physics, University of Colorado, Boulder, CO 80309, USA

³Shenzhen Institute for Quantum Science and Technology and Department of Physics, Southern University of Science and Technology, Shenzhen, 518055, China

⁴Department of Physics, University of California, Santa Cruz, CA 95064, USA

⁵Neutron Scattering Division, Oak Ridge National Laboratory, Oak Ridge, Tennessee 37831, USA

⁶Center for Quantum Computing, Peng Cheng Laboratory, Shenzhen 518055, China

⁷Center for Experiments on Quantum Materials, University of Colorado, Boulder, CO 80309, USA

* nini@physics.ucla.edu

† dessau@colorado.edu

‡ liugh@sustech.edu.cn

ABSTRACT

Magnetic topological insulators provide an important materials platform to explore emergent quantum phenomena such as the quantized anomalous Hall (QAH) effect, Majorana modes and the axion insulator state, etc. Recently, MnBi_2Te_4 was discovered to be the first material realization of a van der Waals (vdW) antiferromagnetic topological insulator (TI). In the two-dimensional (2D) limit, at a record high temperature of 4.5 K, MnBi_2Te_4 manifests the QAH effect in the forced ferromagnetic state above 12 T. To realize the QAH effect at lower fields, it is essential to search for magnetic TIs with lower saturation fields. By realizing a bulk vdW material MnBi_4Te_7 with alternating $[\text{MnBi}_2\text{Te}_4]$ and $[\text{Bi}_2\text{Te}_3]$ layers, we suggest that it is ferromagnetic in plane but antiferromagnetic along the c axis with a small out-of-plane saturation field of ~ 0.22 T at 2 K. Our angle-resolved photoemission spectroscopy and first-principles calculations further demonstrate that MnBi_4Te_7 is a Z_2 antiferromagnetic TI with two types of surface states associated with the $[\text{MnBi}_2\text{Te}_4]$ or $[\text{Bi}_2\text{Te}_3]$ termination, respectively. Therefore, MnBi_4Te_7 provides a new material platform to investigate emergent topological phenomena associated with the QAH effect at much lower magnetic fields in its 2D limit.

Introduction

Magnetic topological insulators (MTI), including Chern insulators with a Z -invariant and antiferromagnetic (AFM) topological insulators (TIs) with a Z_2 -invariant, provide fertile ground for the exploration of emergent quantum phenomena such as the quantum anomalous Hall (QAH) effect, Majorana modes, the topological magnetoelectric effect, the proximity effect, etc^{1,2}. Although the QAH effect has been experimentally realized in magnetically doped topological insulator $\text{Cr}_{0.15}(\text{Bi}_{0.1}\text{Sb}_{0.9})_{1.85}\text{Te}_3$ thin films³, the unavoidable sample inhomogeneity in doped materials restrains the investigation of associated emergent phenomena under strict experimental conditions. Stoichiometric MTIs are expected to have homogeneous electronic and magnetic properties, which may provide new opportunities to study the QAH effect. Recently, MnBi_2Te_4 was discovered to be an intrinsic AFM TI⁴⁻¹⁸. In its two-dimensional (2D) limit, quantized Hall conductance originating from the topological protected chiral edge states was realized in odd number of slabs¹⁶. However, probably because the uncompensated single FM layer cannot provide enough Zeeman field to realize the band inversion in only one spin channel, to observe such a QAH effect, a magnetic field of 12 T at 4.5 K or 6 T at 1.5 K is required to fully polarize the AFM spins into a forced ferromagnetic (FM) state¹⁶.

How can we achieve the QAH effect at much lower magnetic fields in AFM TIs so that the associated emergent phenomena could be studied at more accessible conditions and the quantized Landau levels would not contaminate the QAH effect? Since a forced FM state is crucial to realize the QAH effect in MnBi_2Te_4 ¹⁶, a MTI with low saturation fields is highly desirable. Recall that MnBi_2Te_4 is a van der Waals (vdW) material crystalizing in the GeBi_2Te_4 structure with septuple (SL) layers of $[\text{Te-Bi-Te-Mn-Te-Bi-Te}]$. Hence, one strategy to achieve small saturation fields is to reduce the interlayer Mn-Mn exchange interaction by increasing the interlayer distance with extra spacer layers in between the SL blocks. Structurally, SL blocks have great compatibility with quintuple (QL) blocks of $[\text{Bi}_2\text{Te}_3]$, whose bulk form is a time-reversal-invariant TI¹⁹. As an example, GeBi_4Te_7 with alternating $[\text{GeBi}_2\text{Te}_4]$ and $[\text{Bi}_2\text{Te}_3]$ building blocks has been synthesized¹⁹. This superior compatibility provides us with flexible structural control to achieve our goal. Furthermore, not only can such superlattices manifest weak interlayer magnetic coupling, but they can

also become natural heterostructures in their 2D limit.

The exploration of the MnTe-Bi₂Te₃ ternary system²⁰ has shown that MnBi_{2n}Te_{3n+1} ($n = 1, 2$ and 3) series exist with alternating [MnBi₂Te₄] and n [Bi₂Te₃] layers. In this work, we focus on MnBi₄Te₇ ($n = 2$) with a hexagonal superlattice crystal structure of alternate stacking of one [MnBi₂Te₄] SL and one [Bi₂Te₃] QL, as shown in Fig. 1(a). Through our transport, thermodynamic, angle-resolved photoemission spectroscopy (ARPES) and first-principles calculations, we discovered that MnBi₄Te₇ is a Z₂ AFM TI with an out-of-plane saturation field as low as 0.22 T, 40 times lower than that of MnBi₂Te₄. Our finding provides a superior new material realization to explore the QAHE and associated phenomena.

Results

A-type antiferromagnetism in MnBi₄Te₇ with strong FM fluctuations and weak interlayer exchange interaction. Figure 1(b) shows the (0 0 l) x-ray diffraction peaks of a representative crystal, which can be well indexed by the MnBi₄Te₇ crystal structure²⁰. The inset of Fig. 1(b) shows a picture of a MnBi₄Te₇ single crystal against a 1-mm scale, where the shiny cleaved ab surface can be seen.

The magnetic properties are depicted in Figs. 1(c)-(e). The data show a dominant FM mean field. By analogy to other layered systems, the Mn moments presumably order in the A-type AFM structure with c axis as the magnetic easy axis, as shown in Fig. 1(a). Furthermore, MnBi₄Te₇ has much weaker interlayer exchange interaction than that of MnBi₂Te₄.

Figure 1(c) presents the field-cooled (FC) magnetic susceptibility data of χ^{ab} ($H \parallel ab$) and χ^c ($H \parallel c$) measured at 0.1 T. The abrupt halt in the rise of χ^c on cooling suggests the onset of AFM ordering, similar to that seen in the other vdW antiferromagnets MnBi₂Te₄ and CrCl₃,^{9,18,21} but different from the FM one²², suggesting that long range AFM ordering takes place at 12 K. Fitting the susceptibilities up to 80 K to the Curie-Weiss law results in Weiss temperatures of $\theta_w^{ab} = 11.5$ K, $\theta_w^c = 12.2$ K, $\theta_w^{ave} = 11.7$ K, and

effective moments of $\mu_{eff}^{ab} = 5.4\mu_B/\text{Mn}$, $\mu_{eff}^c = 5.1\mu_B/\text{Mn}$ and $\mu_{eff}^{ave} = 5.3\mu_B/\text{Mn}$. These values suggest magnetic isotropy above T_N and thus negligible single ion anisotropy in the material. Despite the fact that MnBi_4Te_7 is AFM below 12 K, the positive θ_w^{ave} of 11.7 K suggests strong ferromagnetic (FM) exchange interactions. Recall that MnBi_2Te_4 has a much higher T_N of 25 K and a much lower θ_w of 3~6 K^{9,18}, this may indicate that the energy scales of the FM and AFM exchange interaction are much closer in MnBi_4Te_7 . This is consistent with the fact that the extra insulating $[\text{Bi}_2\text{Te}_3]$ layer reduces the interlayer exchange interaction as we initially anticipated. Indeed, our first-principle calculations also reveal an A-type AFM configuration in MnBi_4Te_7 with the interlayer exchange coupling about -0.15 meV/Mn, which is about one order of magnitude smaller than the counterpart of MnBi_2Te_4 . More details are given in Supplementary Note II.

Figures 1(d)-(e) present the hysteresis loop of isothermal magnetization data for $M^c(H)$ ($H \parallel c$) and $M^{ab}(H)$ ($H \parallel ab$), respectively. As shown in Fig. 1(d), at higher fields, in sharp contrast to MnBi_2Te_4 where a spin-flop transition takes place at 3.5 T and saturates at 8 T in $M^c(H)$ ($H \parallel c$)^{9,17}, MnBi_4Te_7 undergoes a first-order spin-flip transition with hysteresis starting at a much lower field of $H_f = 0.15$ T. It quickly enters the forced FM state and saturates at $H_c = 0.22$ T. Upon warming up to 10 K, the hysteresis area is gradually reduced to zero, but H_c remains little changed, indicating a sharp triggering of the spin-flipping between 10 K and T_N . The spin-flipping also takes place at 2 K in $M^{ab}(H)$ as shown in Fig. 1 (e), but at a higher field of $H_f = 0.4$ T and $H_c = 0.55$ T with a smaller hysteresis area, suggesting the c axis as the magnetic easy axis. The low ordering temperature and small saturation field again indicate weaker interlayer AFM exchange interaction than in MnBi_2Te_4 . The saturation moment is $3.1\mu_B/\text{Mn}$, which is slightly smaller than $3.6\mu_B/\text{Mn}$ ^{9,18} in MnBi_2Te_4 , but much larger than $1.5 \mu_B/\text{Mn}$ in MnSb_2Te_4 ¹⁸. The reduced Mn saturation moments in this family may be due to the deviation of the Mn-Te bond from being perfectly ionic.

Figure 1(f) shows the temperature dependent in-plane (ρ_{xx}) and out-of-plane resistivity (ρ_{zz}). Above 20 K, both ρ_{xx} and ρ_{zz} decrease nearly linearly upon cooling with $\rho_{zz}/\rho_{xx} \sim 53$ at 300 K (Fig. S2), suggesting a large transport anisotropy which is consistent with its

vdW nature. With further cooling, ρ_{xx} and ρ_{zz} increase slightly, which is likely caused by the enhanced scattering from spin fluctuations, a phenomenon frequently observed in low dimensional magnetic materials^{24,25}. Then at 12 K, a sudden drop of ρ_{xx} and a sharp increase of ρ_{zz} are observed. This is in agreement with the A-type magnetic structure shown in Fig. 1(a) since the antiparallel alignment of Mn moments can reduce the conductivity via spin-slip scattering, while parallel alignment of the Mn moments will eliminate such scattering and thus enhance the conductivity²⁴.

The existence of strong FM spin fluctuations up to 50 K manifests in Fig. 1 (g), which shows the transverse magnetoresistance (TMR), defined as $MR = (\rho_{xx}(H) - \rho_{xx}(0))/\rho_{xx}(0)$, and measured up to 9 T at various temperatures up to 50 K. The main feature of the figure is the overall "W" shape of the TMR. The "W" shape becomes deeper with increasing temperature, with the largest negative TMR of 8% appearing at 12 K, which corresponds to T_N . Above T_N , it starts to become shallower and finally transforms into an ordinary parabolic shape at 50 K. The overall "W" shape can be understood in the framework of FM fluctuations. Above 50 K, the lack of magnetic fluctuations leads to the parabolic TMR. Upon cooling, FM fluctuations begin to appear and become increasingly stronger with maxima around T_N . As a result, the summation of the positive parabolic TMR and the negative TMR arising from the FM fluctuations under fields leads to a progressively deeper "W" shape of TMR upon cooling. Below T_N , the FM fluctuations are reduced, but still with a strong presence, leading to the shallower "W" shape under field.

The spin-flip transition strongly affects the transport properties, as shown in Fig. 2. $\rho_{xx}(H)$, $\rho_{zz}(H)$ and $\rho_{xy}(H)$ follow the same hysteresis as that in $M(H)$. For $H \parallel c$, ρ_{xx} slightly changes between 0 T to H_f . It then sharply drops by 3.8% up to H_c since the system enters the forced FM state and the loss of spin scattering occurs. For $H \parallel ab$, a giant negative magnetoresistance associated with the spin-flip transition was observed. ρ_{zz} monotonically decreases by 10% from 0 T to H_f , followed by a sudden 14% drop up to H_c . The system displays evident anomalous Hall effect (AHE) as seen in the bottom panel of Fig. 2(a). Our $\rho_{xy}(H)$ is linear up to 9 T above 50 K (Fig. S3) suggesting single band transport here. Using $n = H/e\rho_{xy}$, our 50 K data corresponds to an electron carrier

density of $2.84 \times 10^{20} \text{ cm}^{-3}$, similar to that of MnBi_2Te_4 ^{17, 18, 23}. Our Hall resistivity below 12 K can be described by $\rho_{xy} = R_0H + \rho_{xy}^A$, where the R_0H is the trivial linear contribution and ρ_{xy}^A represents the anomalous Hall resistivity. At 2 K, ρ_{xy}^A is extracted to be $3.3 \mu\Omega \text{ cm}$, which is half of the one in MnBi_2Te_4 ¹⁷. Consequently, the anomalous Hall conductivity $\sigma_{xy}^A (= \rho_{xy}^A / \rho_{xx}^2)$ is $25.5 \Omega^{-1} \text{ cm}^{-1}$ and the anomalous Hall angle (AHA $\sim \rho_{xy}^A / \rho_{xx}$) is $\sim 1\%$.

Z_2 AFM TI predicted by theoretical calculation. MnBi_4Te_7 crystalizes in space group (G) $P\bar{3}m1$ (No. 164). By taking into account the A-type antiferromagnetism, the primitive cell doubles along the c axis, rendering a magnetic space group $Pc\bar{3}c1$ (No. 165.96) under the Belov-Neronova-Smirnova notation²⁶, as shown in Fig. 1(a). This magnetic space group is derived from its nonmagnetic space group by adding an extra sublattice generated by an operation that combines time-reversal T with a fractional translation $\tau_{1/2}$. Then the full magnetic group is built as $G_M = G + GS$, where S is a combinatory symmetry $S = T\tau_{1/2}$ with $\tau_{1/2}$ the half translation along the c axis of the AFM primitive cell. Although the explicit T -symmetry is broken, the S symmetry (also referred to nonsymmorphic time-reversal²⁷) still exists in bulk MnBi_4Te_7 . In addition, MnBi_4Te_7 has inversion symmetry P , while the square of the symmetry operator PS equals to -1 at an arbitrary k in momentum space. Therefore, analogous to TI with T -symmetry where Kramer's degeneracy is induced by $T^2 = -1$, in MnBi_4Te_7 the existence of the PS symmetry ensures an equivalent Kramer's degeneracy in the whole Brillion zone, and thus a Z_2 topological classification.

Figure 3(a) shows the calculated band structure of bulk AFM MnBi_4Te_7 with the presence of spin-orbit coupling. The conduction band minimum is located at the Γ point, while the valence band maximum in the vicinity of Γ shows a slightly curved feature. The bulk band gap is about 0.16 eV. The projection of band eigenstates onto the p -orbitals of Bi and Te (as indicated by the green and red coloring) clearly indicates an inverted order between several conduction and valence bands around the Γ point, which is strong evidence of the possible nontrivial topological nature. On the other hand, the Mn- $3d^5$ states form nearly

flat bands far away from the Fermi level (see Supplementary Fig. S5), indicating that the main effect of Mn is to break T -symmetry by introducing staggered Zeeman field into the low-energy Hamiltonian. The calculated magnetic moment is about $4.6 \mu_B/\text{Mn}$.

To determine the topological properties of AFM MnBi_4Te_7 , we first apply the Fu-Kane formula²⁸ to calculate the Z_2 invariant. Four TRIM points, including $\Gamma(0, 0, 0)$ and three equivalent $M(\pi, 0, 0)$, need to be considered here with $\mathbf{k} \cdot \boldsymbol{\tau}_{1/2} = n\pi$. Due to the abovementioned band inversion at the Γ point, we find that the parities for the occupied bands at Γ is opposite to that of the other three M points, indicating a nontrivial $Z_2 = 1$. To verify our results, we also calculate the evolution of Wannier charge centers (WCCs) using the Wilson loop approach²⁹. As show in Fig. 3(b), the largest gap function and the WCCs line cross each other odd number of times through the evolution, confirming that MnBi_4Te_7 is indeed a Z_2 AFM topological insulator. Compared with TIs with T -symmetry, the protection of gapless surface states in AFM TIs requires that the cleaved surface respects S symmetry that contains translation along the c axis. Figure 3(c) clearly shows the gapless surface Dirac cone at the Γ point for the (010) surface, partially validating the bulk-surface correspondence of MnBi_4Te_7 as an AFM TI. We note that the easy-cleaved (001) surface states, where the S symmetry is broken, are measured by ARPES compared with our theoretical calculations, as discussed in the following.

Gapped (001) surface states measured by ARPES. In contrast to the recently discovered AFM TI MnBi_2Te_4 where only one type of surface termination exists, MnBi_4Te_7 could terminate on two different sub-lattice surfaces on the (001) plane, i.e., the $[\text{Bi}_2\text{Te}_3]$ QL termination and the $[\text{MnBi}_2\text{Te}_4]$ SL termination, resulting in different topological surface states. On these two terminations, symmetry operations combined with $\tau_{1/2}$ are not preserved. Due to the out-of-plane magnetization of the Mn sublayers, the gapped surface states are described by adding an exchange term to the ordinary Rashba-type surface Hamiltonian for TI with T symmetry, i.e., $H_{\text{surf}}(\mathbf{k}) = (\sigma_x k_y - \sigma_y k_x) + m_{t/b} \sigma_z$, where σ is the Pauli matrix for spin, and $m_{t/b}$ the surface exchange field that distinguishes the $[\text{MnBi}_2\text{Te}_4]$ SL and $[\text{Bi}_2\text{Te}_3]$ QL surfaces. Our calculation results show that the surface state terminated at the $[\text{MnBi}_2\text{Te}_4]$ SL has a massive Dirac cone with a gap around 40 meV [see

Fig. 4(a)]. On the other hand, the upper Dirac cone of the $[\text{Bi}_2\text{Te}_3]$ QL termination goes deeper down in energy and merges with the bulk valence band. The differences of surface spectra, which can be attributed to the difference of exchange field and surface potential between the two terminations, serve as a unique feature of the superlattice-like MnBi_4Te_7 for ARPES measurements.

Indeed, under the same experimental conditions, we consistently observed two types of ARPES spectra on different parts of the sample in real space, as plotted in Fig. 4(b) and Fig. 4(e). The corresponding curvature method plots are shown in Fig. 4(c) and Fig. 4(f) for reference. To the first order, these two spectra show similar features, including strong intensity on the electron pockets and Dirac-cone like surface states with much weaker intensity. We interpret these two as spectra from the $[\text{MnBi}_2\text{Te}_4]$ SL termination and the $[\text{Bi}_2\text{Te}_3]$ QL termination, respectively, whose different surface conditions modify the visibility of the bands via the matrix element effect. Since the upper Dirac-cone like feature in Fig. 4(e) goes deeper into the valence band than that in Fig. 4(b), we suggest that the spectra arise from the $[\text{Bi}_2\text{Te}_3]$ termination. Taken together, the ARPES measurements confirm the DFT calculation of these two topological surface states.

Figure 5 shows typical examples of the iso-energy plots observed under synchrotron light of 90 eV. Above the Dirac point, DFT calculations predict multiple six-fold bulk band electron pockets because of the hexagonal warping effect³⁰ [Fig. 5(a)]. However, only the inner pockets are clearly observed in our experimental spectra, as shown in Fig. 5(b), while the snowflake-like outer pockets are absent from our ARPES observations, likely due to the matrix element effect. Below the Dirac point, ARPES observes multiple snowflake-like hole pockets in the bulk bands [Fig. 5(d)], which show good agreement with our DFT calculations [Fig. 5(c)].

Discussion

vdW materials are the foundation of engineering 2D heterostructures, which have recently opened up unprecedented opportunities in discovering new physics as well as making new quantum devices³¹. The 2D version exfoliated from bulk vdW TI paves an avenue to chase

the long-sought emergent properties such as QAH effect and quantum spin Hall effect. AFM TI MnBi_2Te_4 in its 2D limit is predicted to exhibit an oscillation between QAH insulator and zero-plateau QAH insulator for odd and even number of SLs, respectively, when the sample is thicker than 3SLs¹³. This prediction has recently been experimentally observed in atomic-thin MnBi_2Te_4 ^{16,32} at 12 T and 4.5 K or 6 T at 1.5 K.

The vdW AFM TI MnBi_4Te_7 single crystal reported here is in fact a 1:1 superlattice composing the building blocks of AFM TI $[\text{MnBi}_2\text{Te}_4]$ and T -invariant TI $[\text{Bi}_2\text{Te}_3]$. Our realization of the superlattice design has three advantages. First, as discussed above, it serves as a “buffer layer” that separates and thus effectively decreases the AFM coupling between the two neighboring $[\text{MnBi}_2\text{Te}_4]$ SLs, leading to a weaker magnetic field to trigger the QAH. Second, by interlayer coupling between $[\text{Bi}_2\text{Te}_3]$ QL and adjacent $[\text{MnBi}_2\text{Te}_4]$ SLs, the SOC-induced nontrivial topology of $[\text{Bi}_2\text{Te}_3]$ ensures the band inversion in the 2D limit. As a result, QAH is well expected in few-layer MnBi_4Te_7 . Third, when MnBi_4Te_7 is exfoliated into the 2D limit, natural heterostructures are made, which provides more 2D configurations than MnBi_2Te_4 or Bi_2Te_3 since the latter ones are only stacked by one type of building block.

In summary, MnBi_4Te_7 is a bulk van der Waals superlattice of alternating $[\text{Bi}_2\text{Te}_3]$ and $[\text{MnBi}_2\text{Te}_4]$ layers. It is ferromagnetic in plane but antiferromagnetic along the c axis below 12 K with an out-of-plane saturation field as low as 0.22 T at 2 K. Based on our first-principles calculations and angle-resolved photoemission spectroscopy measurements, we show that it is a Z_2 antiferromagnetic topological insulator with two distinct (001) surface states from $[\text{Bi}_2\text{Te}_3]$ and $[\text{MnBi}_2\text{Te}_4]$ termination, respectively. Due to its superlattice nature, in the two-dimensional limit, it serves as natural heterostructures. The extremely low saturation field thus makes it an ideal system to study the quantized anomalous Hall effect, quantum spin Hall effect and associated emergent phenomena.

Methods

Sample growth and characterization. Single crystals of MnBi_4Te_7 were grown using self-flux¹¹. Although Bi_2Te_3 is the inevitable side product, we can differentiate MnBi_4Te_7 pieces

by measuring their $(0\ 0\ l)$ diffraction peaks. In each growth, a few sizable plate-like MnBi_4Te_7 single crystals with typical dimensions of $3 \times 3 \times 0.5\ \text{mm}^3$ were obtained. To confirm the phase, X-ray diffraction data were collected using a PANalytical Empyrean diffractometer (Cu $K\alpha$ radiation). Samples used for powder X-ray diffraction were ground into powder inside acetone solution to reduce the preferred orientation. Electric resistivity and heat capacity data were measured in a Quantum Design (QD) DynaCool Physical Properties Measurement System (DynaCool PPMS). The magnetization data were measured in a QD Magnetic Properties Measurement System (QD MPMS). All magnetic data were calculated assuming the molar ratio between MnBi_4Te_7 and Bi_2Te_3 flux is 86 : 14 in the sample suggested by powder X-ray refinement (Fig. S1). Magnetic data measured for $H \parallel c$ were corrected with a demagnetization factor.

ARPES measurements. ARPES measurements on single crystals of MnBi_4Te_7 have been carried out at the Advanced Light Source beamline 7.0.2 with combinations of multiple photon energies from 60 eV to 120 eV and polarization of linear horizontal, circular left or circular right. Single crystal samples were top-posted on the $[001]$ surface, and cleaved in-situ in an ultra-high vacuum better than 4×10^{-11} Torr and a temperature of 50 K. ARPES spectra were taken at 11 K, slightly below the Neel temperature. As the cleaved terrain is expected to consist of patches of exposed $[\text{Bi}_2\text{Te}_3]$ QL layers and the $[\text{MnBi}_2\text{Te}_4]$ SL layers, the beam spot size was limited to 30 by 20 μm^2 to better distinguish their corresponding spectra.

First-principles calculations. We apply density functional theory (DFT) by using the projector-augmented wave (PAW) pseudopotentials³⁴ with the exchange-correlation of Perdew-Burke-Ernzerhof (PBE) form³⁵ and GGA+U³⁶ approach within the Dudarev scheme³⁷ as implemented in the Vienna ab-initio Simulation Package (VASP)³⁸. The energy cutoff is chosen 1.5 times as large as the values recommended in relevant pseudopotentials. The U value is set to be 5 eV, which is tested by Ref. [6]. The k-points-resolved value of BZ sampling is $0.02 \times 2\pi/\text{\AA}$. The total energy minimization is performed with a tolerance of 10^{-6} eV. The crystal structure is fully relaxed until the atomic force on each atom is less than 10^{-2} eV \AA . SOC is included self-consistently throughout the calculations. We constructed Wannier representations^{39,40} by projecting the Bloch states from the DFT calculations of bulk materials onto the Mn-3*d*, Bi-6*p* and Te-5*p* orbitals. The band spectra

of the surface states are calculated in the tight-binding models constructed by these Wannier representations and by the iterative Green's function technique as implemented in WannierTools package⁴¹.

Acknowledgments

We thank Paul C. Canfield, Dr. Quansheng Wu, Suyang Xu, Filip Ronning and Chris Regan for helpful discussions, and Chris Jozwiak and Roland Koch at the Advanced Light Source for experimental help. Work at UCLA, the University of Colorado and UCSC were supported by the U.S. Department of Energy (DOE), Office of Science, Office of Basic Energy Sciences under Award Number DE-SC0011978, DE-FG02-03ER46066 and DE-SC0017862, respectively. Work at SUSTech was supported by the NSFC under Grant No. 11874195. HC acknowledges the support from US DOE BES Early Career Award KC0402010 under Contract DE-AC05-00OR22725. This research used resources of the Advanced Light Source, which is a DOE Office of Science User Facility under contract no. DE-AC02-05CH11231.

Author contributions

N. N. conceived the idea and organized the research. N. N., Q. L. and D. D. supervised the research. C. H., J. L., E. E., H. B. and N. N. grew the bulk single crystal and carried out X-ray and transport measurements. X. Z., P. H. and D. D. carried out the ARPES measurements and data analysis. Q. L., P. L., H. S. and Y. L. performed the first-principles calculations. A. R. performed magnetic measurements. H. C. carried out neutron scattering measurements. N. N., Q. L. and X. Z. prepared the manuscript with contributions from all authors.

1. Mong, R. S. K., Essin, A. M. & Moore, J. E. Antiferromagnetic topological insulators. *Phys. Rev. B* **81**, 245209 (2010).
2. Tokura, Y., Yasuda, K. & Tsukazaki, A. Magnetic topological insulators. *Nat. Rev. Phys.* **1** (2019).
3. Chang, C.-Z. *et al.* Experimental observation of the quantum anomalous Hall effect in

- a magnetic topological insulator. *Science* **340**, 167–170 (2013).
4. Hirahara, T. *et al.* Large-gap magnetic topological heterostructure formed by subsurface incorporation of a ferromagnetic layer. *Nano Lett.* **17**, 3493 (2017).
 5. Hagmann, J. A. *et al.* Molecular beam epitaxy growth and structure of self-assembled Bi₂Se₃/Bi₂MnSe₄ multilayer heterostructures. *New J. Phys.* **19**, 085002 (2017).
 6. Otrokov, M. M. *et al.* Highly-ordered wide bandgap materials for quantized anomalous Hall and magnetoelectric effects. *2D Mater.* **4**, 025082 (2017).
 7. Gong, Y. *et al.* Experimental realization of an intrinsic magnetic topological insulator. *ArXiv Prepr. ArXiv1809.07926* (2018).
 8. Lee, D. S. *et al.* Crystal structure, properties and nanostructuring of a new layered chalcogenide semiconductor, Bi₂MnTe₄. *CrystEngComm* **15**, 5532 (2013).
 9. Otrokov, M. M. *et al.* Prediction and observation of the first antiferromagnetic topological insulator. *ArXiv Prepr. ArXiv1809.07389* (2018).
 10. Zeugner, A. *et al.* Chemical Aspects of the Candidate Antiferromagnetic Topological Insulator MnBi₂Te₄. *Chem. Mater.* (2019).
 11. Yan, J.-Q. *et al.* Crystal growth and magnetic structure of MnBi₂Te₄. *ArXiv Prepr. ArXiv: 1902.10110* (2019).
 12. Chen, B. *et al.* Searching the Mn (Sb, Bi)₂Te₄ family of materials for the ideal intrinsic magnetic topological insulator. *ArXiv Prepr. ArXiv:1903.09934* (2019).
 13. Otrokov, M. *et al.* Unique Thickness-Dependent Properties of the van der Waals Interlayer Antiferromagnet MnBi₂Te₄ Films. *Phys. Rev. Lett.* **122**, 107202 (2019).
 14. Zhang, D. *et al.* Topological axion states in magnetic insulator MnBi₂Te₄ with the quantized magnetoelectric effect. *ArXiv Prepr. ArXiv: 1808.08014* (2018).

15. Li, J. *et al.* Intrinsic magnetic topological insulators in van der Waals layered MnBi₂Te₄-family materials. *ArXiv Prepr. ArXiv:1808.08608* (2018).
16. Deng, Y. *et al.* Magnetic-field-induced quantized anomalous Hall effect in intrinsic magnetic topological insulator MnBi₂Te₄. *ArXiv Prepr. ArXiv:1904.11468* (2019).
17. Lee, S. H. *et al.* Spin scattering and noncollinear spin structure-induced intrinsic anomalous Hall effect in antiferromagnetic topological insulator MnBi₂Te₄. *ArXiv Prepr. ArXiv: 1812.00339* (2018).
18. Yan, J. *et al.* Evolution of structural, magnetic and transport properties in MnBi_{2-x}Sb_xTe₄. *ArXiv Prepr. ArXiv: 1905.00400* (2019).
19. Muff, S. *et al.* Separating the bulk and surface n-to p-type transition in the topological insulator GeBi_{4-x}Sb_xTe₇. *Phys. Rev. B* **88**, 035407 (2013).
20. Aliev, Z. S. *et al.* Novel ternary layered manganese bismuth tellurides of the MnTe-Bi₂Te₃ system: Synthesis and crystal structure. *J. Alloys Compd.* (2019).
21. McGuire M. A., *et al.*, Magnetic behavior and spin-lattice coupling in cleavable van der Waals layered CrCl₃ crystals, *Phys. Rev. Materials* **1**, 014001 (2017).
22. Liu, Y., Stavitski, E., Attenkofer, K., Petrovic, C., Anomalous Hall effect in the van der Waals bonded ferromagnet Fe_{3-x}GeTe₂. *Phys. Rev. B* **97**, 165415 (2018).
23. Cui, J. *et al.* Transport properties of thin flakes of the antiferromagnetic topological insulator MnBi₂Te₄. *Phys. Rev. B* **99**, 155125 (2019).
24. Masuda, H. *et al.* Quantum Hall effect in a bulk antiferromagnet EuMnBi₂ with magnetically confined two-dimensional Dirac fermions. *Sci. Adv.* **2**, e1501117 (2016).
25. Shen, B. *et al.* Structural distortion and incommensurate noncollinear magnetism in EuAg₄As₂. *ArXiv Prepr. ArXiv: 1809.07317* (2018).

26. Belov, N., Neronova, N. & Smirnova, T. Shubnikov groups. *Kristallografiya* **2**, 315–325 (1957).
27. Hua, G. *et al.* Dirac semimetal in type-IV magnetic space groups. *Phys. Rev. B* **98**, 201116 (2018).
28. Fu, L. & Kane, C. L. Topological insulators with inversion symmetry. *Phys. Rev. B* **76**, 045302 (2007).
29. Soluyanov, A. A. & Vanderbilt, D. Computing topological invariants without inversion symmetry. *Phys. Rev. B* **83**, 235401 (2011).
30. Fu, L. Hexagonal Warping Effects in the Surface States of the Topological Insulator Bi₂Te. *Phys Rev Lett* **103**, 266801 (2009).
31. Geim, A. K. & Grigorieva, I. V. Van der Waals heterostructures. *Nature* **499**, 419 (2013).
32. Liu, C. *et al.* Quantum phase transition from axion insulator to Chern insulator in MnBi₂Te₄. *ArXiv Prepr. ArXiv: 1905. 00715* (2019).
33. Hongyi Sun, Pengfei Liu, Qihang Liu, et al., in preparation, (2019).
34. Kresse, G. & Joubert, D. From ultrasoft pseudopotentials to the projector augmented-wave method. *Phys. Rev. B* **59**, 1758 (1999).
35. Perdew, J. P., Burke, K. & Ernzerhof, M. Generalized Gradient Approximation Made Simple. *Phys Rev Lett* **77**, 3865–3868 (1996).
36. Anisimov, V. I., Zaanen, J. & Andersen, O. K. Band theory and Mott insulators: Hubbard U instead of Stoner I. *Phys. Rev. B* **44**, 943 (1991).
37. Dudarev, S., Botton, G., Savrasov, S., Humphreys, C. & Sutton, A. Electron-energy-loss spectra and the structural stability of nickel oxide: An LSDA+ U study. *Phys. Rev. B* **57**, 1505 (1998).

- 38. Kresse, G. & Furthmüller, J. Efficiency of ab-initio total energy calculations for metals and semiconductors using a plane-wave basis set. *Comput. Mater. Sci.* **6**, 15–50 (1996).
- 39. Mostofi, A. A. *et al.* An updated version of wannier90: A tool for obtaining maximally-localised Wannier functions. *Comput. Phys. Commun.* **185**, 2309–2310 (2014).
- 40. Marzari, N. & Vanderbilt, D. Maximally localized generalized Wannier functions for composite energy bands. *Phys. Rev. B* **56**, 12847 (1997).
- 41. Wu, Q., Zhang, S., Song, H.-F., Troyer, M. & Soluyanov, A. A. WannierTools: An open-source software package for novel topological materials. *Comput. Phys. Commun.* **224**, 405–416 (2018).

Figure 1.

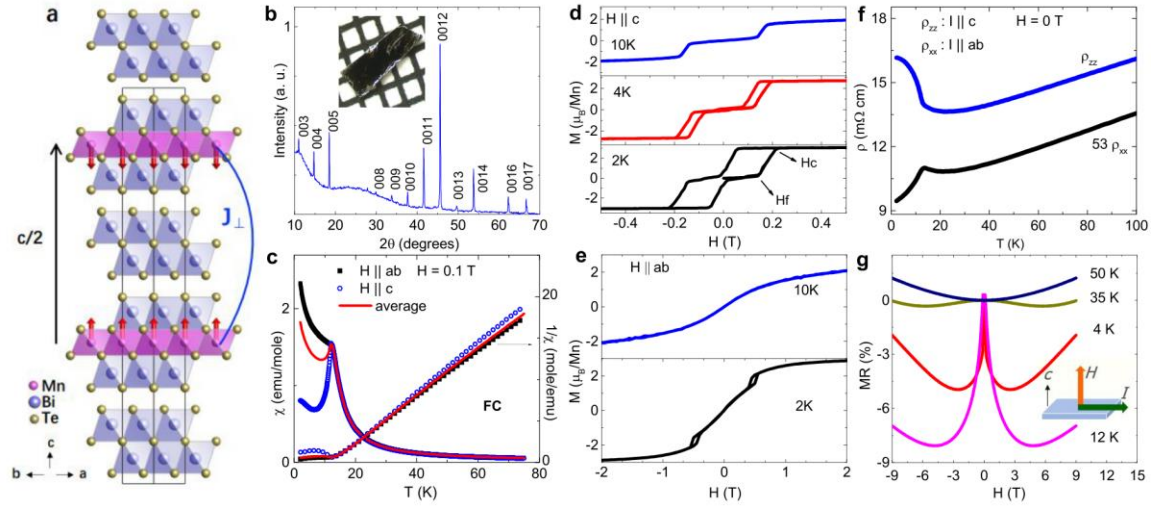


Figure 1. **Magnetic and transport properties of bulk AFM MnBi₄Te₇.** **a** The view of the crystal structure of MnBi₄Te₇ from the [110] directions. Orange arrow: Mn spins in the AFM state. Blue block: edge-sharing BiTe₆ octahedra; Pink block: edge-sharing MnTe₆ octahedra, which are connected to the blue block via edge-sharing. J_{\perp} is the interlayer exchange coupling. **b** The (00 l) X-ray diffraction peaks of the cleaved ab plane of MnBi₄Te₇. Inset: A piece of MnBi₄Te₇ against 1-mm scale. **c** The temperature dependent field-cooled susceptibility and inverse susceptibility taken at $H = 0.1$ T for $H \parallel ab$ and $H \parallel c$. Average χ is calculated by $\chi^{ave} = (2\chi^{ab} + \chi^c)/3$. **d** and **e**: Full magnetic hysteresis loop of isothermal magnetization taken at various temperatures for $H \parallel c$ (**d**) and $H \parallel ab$ (**e**). **f** The temperature dependent ρ_{xx} ($I \parallel ab$) and ρ_{zz} ($I \parallel c$). **g** Transverse magnetoresistance with $I \parallel ab$ and $H \parallel c$ at various temperatures.

Figure 2.

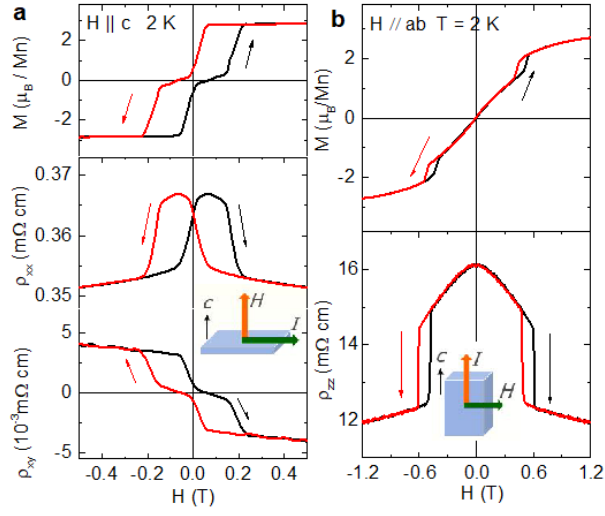


Figure 2. **Magnetotransport of bulk AFM MnBi_4Te_7 .** **a** The field dependent magnetization M , magnetoresistivity ρ_{xx} , and Hall resistivity ρ_{xy} at 2 K with $I \parallel ab$ and $H \parallel c$. **b** The field dependent magnetization M , magnetoresistivity ρ_{xx} , at 2 K with $I \parallel c$ and $H \parallel ab$.

Figure 3.

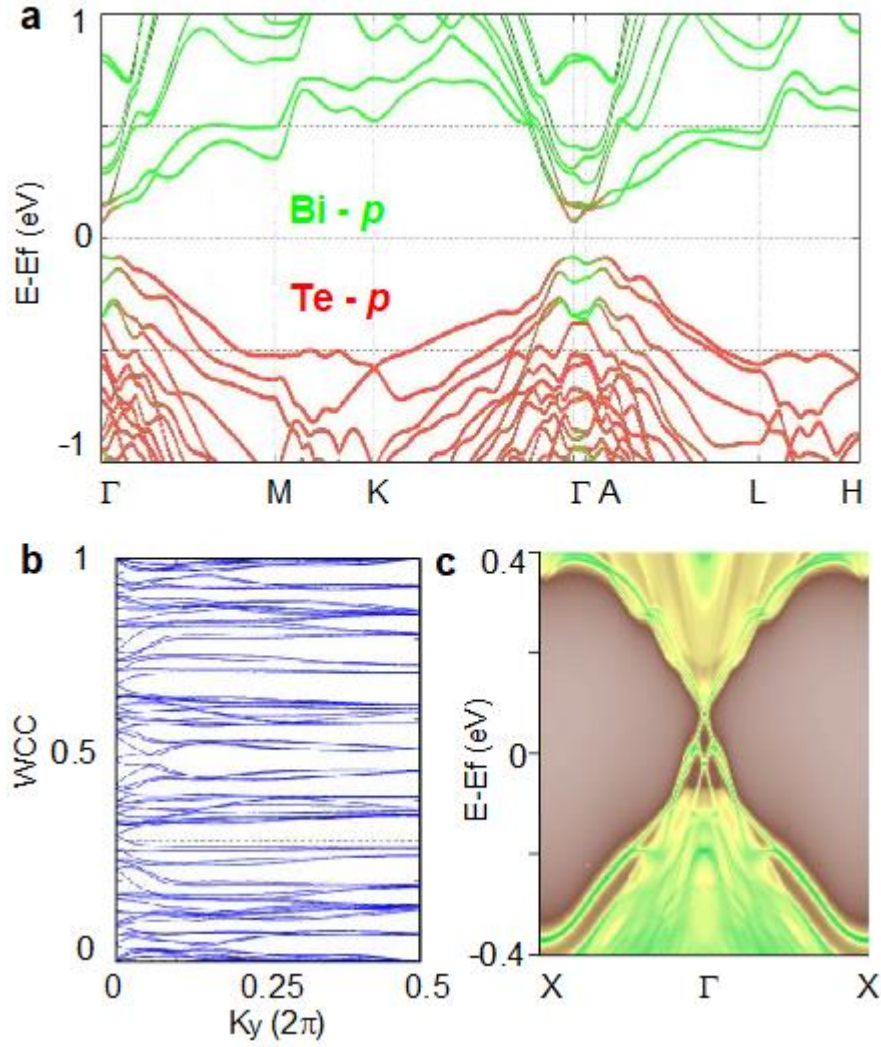


Figure 3 | Topological properties of bulk AFM MnBi_4Te_7 predicted by first-principles calculations. **a** Band structure with the projection of Bloch eigenstates onto Bi-p (green) and Se-p (red) orbitals. SOC is included. **b** Evolution of Wannier charge centers (WCCs) for $k_z = 0$, indicating a nontrivial topological invariant $Z_2 = 1$. **c** Surface spectra of (010) side surface, showing a gapless Dirac cone protected by S symmetry.

Figure 4.

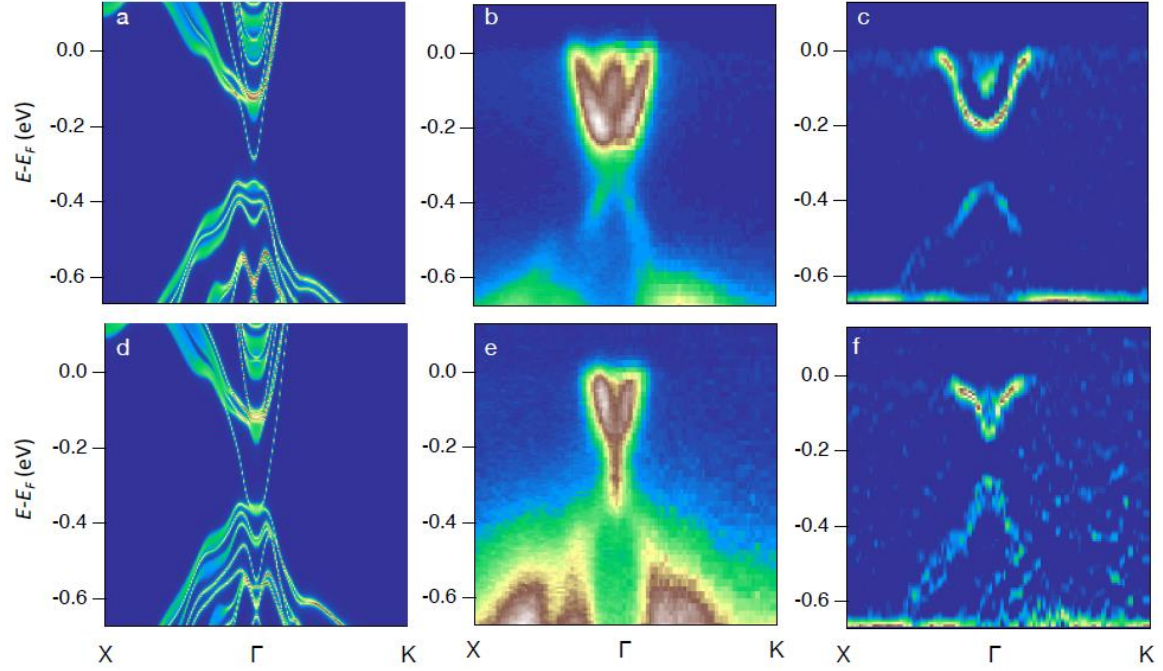


Figure 4 | Comparison between DFT-calculated and ARPES-measured surface states with two different terminations. a, d DFT calculations of surface states of MnBi_4Te_7 for **a** the $[\text{MnBi}_2\text{Te}_4]$ SL termination and **d** $[\text{Bi}_2\text{Te}_3]$ QL termination. To directly compare with ARPES, the Fermi level was shifted down by 270 meV in energy. **b, e** ARPES spectra for **b** the $[\text{MnBi}_2\text{Te}_4]$ SL termination and **e** $[\text{Bi}_2\text{Te}_3]$ QL termination. **c, f** the curvature-method plot of **b** and **e**. DFT calculations and ARPES data show first order agreement.

Figure 5.

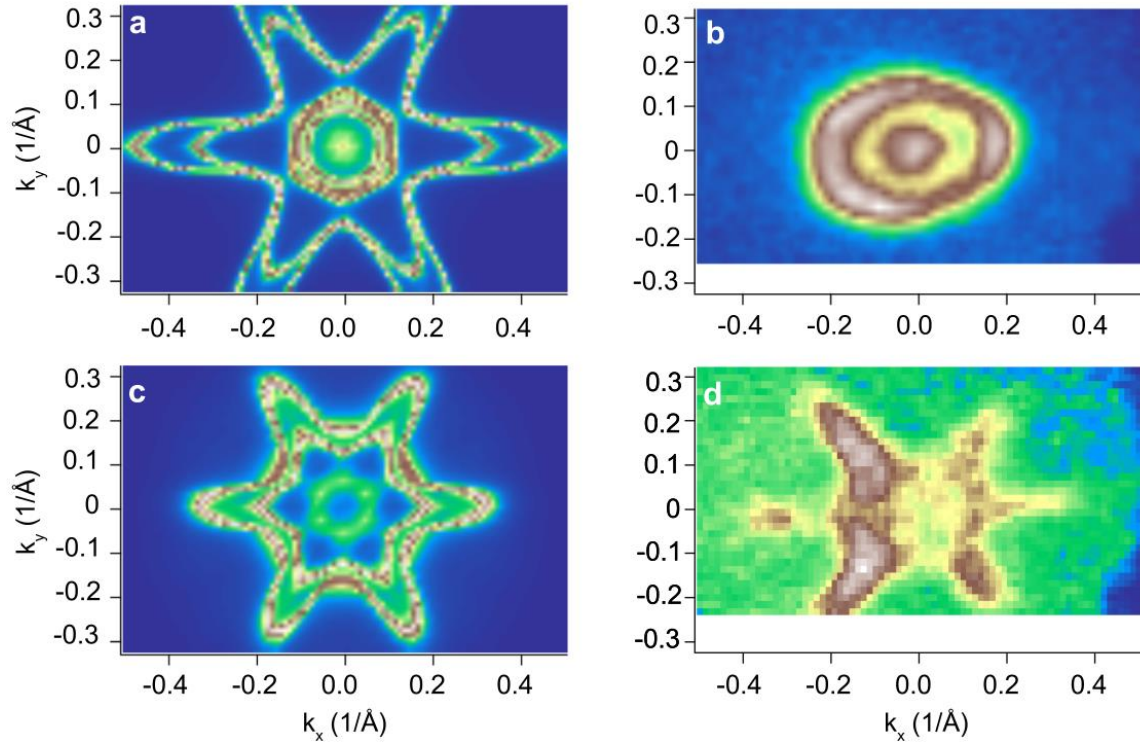


Figure 5 | Iso-energy contours. **a** DFT predicted and **b** ARPES measured iso-energy plot of bulk bands above the Dirac point; **c** DFT predicted and **d** ARPES measured iso-energy plot of bulk bands below the Dirac point.